

# Graph-based Neuron Agglomeration using 3D Skeletons

Anonymous CVPR submission

Paper ID 0446

## Abstract

Advancements in electron microscopy image acquisition have created massive connectomics datasets which are petabytes in size and make manual segmentation not feasible. Proposed methods for automatic segmentations generate super-pixel approximations of neural membranes followed by agglomeration strategies to create full neuron reconstructions. However, pixel-based segmentation results widely neglect global geometric properties. We generate skeletons of membrane labels to approximate neural pathways in 3D. This allows us to efficiently apply graph-based optimization strategies and to train automatic classifiers for shape description against manually labeled ground truth. Our classifiers detect feasible and impossible neural pathways by looking at geometric properties alone, and are able to improve the segmentation labels accordingly. We demonstrate the performance of our classifiers on multiple real-world connectomics datasets with average variation of information improvement of  $X\times$ . We discuss our findings and provide insights to learning shape features for neuron agglomeration.

## 1. Introduction

The field of connectomics is concerned with reconstructing the wiring diagram of the brain at nanometer resolutions. Recent advancements in image acquisition using multi-beam serial-section electron microscopy (sSEM) has allowed neuroscientists to produce terabytes of electron microscopy (EM) image data every hour [13]. Neuroscientists believe that reconstructing an entire mammalian brain at fine resolution will enable new insights into the workings of the brain [18]. These observations will allow for new advancements in neuromedicine and artificial intelligence (CITE). Segmentation is part of this reconstruction process, assigning a unique label for every neuron in the EM image. It is not feasible for domain experts to manually segment the vast amount of 3-D image data to model an entire brain.

A significant amount of research focuses on automatic reconstruction of the neurons in EM images because of the

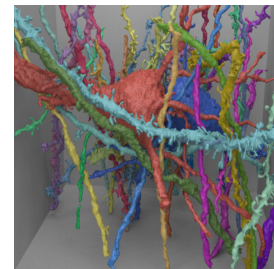
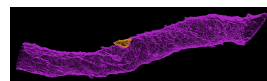


Figure 1: We use 3D skeletons to combine neuron labels to full reconstructions. (TODO: Add schematic figure showing the difference between voxel-based / super-voxel based / graph-based algorithms with connections and hierarchy)

scope and importance of the problem [22, 28, 33, 44]. All of these algorithms extract neuronal processes through the 3-D volumes using only the raw image data as input. Oftentimes, convolutional neural networks (CNNs) predict membrane probabilities or affinities between voxels and apply simple thresholds to agglomerate the voxels into clusters [24, 35]. These *per-voxel* algorithms produce excellent results but currently fall short of complete reconstructions with error rates of approximately  $X\%$ .

Researches currently address the failures of the *per-voxel* algorithms by training random-forest classifiers to agglomerate an oversegmentation of voxels [28] (CITE NEURO-PROOF). These classifiers take the output of the *per-voxel* algorithms as input and generate high-level statistics such as affinity distributions between pixel regions. Presently, these methods use hand-designed features despite the evidence that machine-learned features perform better [4]. These *per-supervoxel* algorithms outperform the *per-voxel* algorithms but still do not provide the accuracy needed for large scale reconstructions of the brain. Additionally, these methods do not fully leverage the wealth of shape information available (e.g., it is well known that neurons angle at less than 30 degrees (CITE)).

Here we present a *graph-based* strategy that builds on top of the outputs of *per-supervoxel* methods by taking neuronal shape properties into account. Similarly we take as

input automatic segmentations. However, we focus on general neuron shapes, traversing through the label volumes to identify potential merge candidates. From these locations we extract machine-learned features and generate a probability that two label segments should be joined. We construct a graph representation of the input label volume. Using graph-based optimization strategies enables us to enforce global constraints that more closely match the underlying biology of the images. Lastly, we apply a globally optimal algorithm to produce a better reconstruction.

## 2. Related Work

**Voxel-based methods.** A large amount of connectomics research considers the problem of extracting segmentation information at the voxel level from the raw EM images to produce label volumes. In a label volume, every voxels receives a segment label corresponding to a unique neuron. Voxels with the same segment label belong to the same neuron. Such works focus on training 2-D convolutional neural networks to predict membrane probabilities per image slice [6, 15, 42, 23, 19]. More recent strategies augment these neural networks with the  $z$ -dimension creating full 3-D convolutional networks [24]. Oftentimes these networks produce probabilities for the affinity between voxels rather than probabilities for a voxel belonging to a cell membrane [35]. A sizable amount of computer vision research analyzes various hand-designed shape features for determining similarity between objects [29] and for segmentation[7]. Currently, the random-forest classifiers used in connectomics rely on hand-designed features to make merge decisions. Some of these features encode the distribution of probabilities that voxels along a segment boundary belong to the same neuron as their neighbors [28, 34]. However, there is evidence that machine-learned features outperform hand-designed ones [4]. An extensive amount of research in computer vision, applied mathematics, and statistics evaluates the loss functions and optimizers for these networks [5, 25, 27].

**Super-voxel methods.** These approaches generate probabilities that neighboring voxels belong to the same neuron. Many algorithms work at the resulting supervoxel level and train random-forest classifiers to produce segmentations of the EM images where every unique neuron in the volume has a unique label [22, 28, 33, 44] (CITE NEUROPROOF). Despite the success of these classifiers, they often make mistakes based on the local information leading to errors in the segmentation. Proofreading methods create a “human-in-the-loop” framework that allows users to find errors and correct them [10, 11, 12, 45].

More recently, flood-filling networks merge the process of generating voxel affinities and then producing segmentations by training an end-to-end neural network that out-

puts segmentations [16]. These networks produce impressive segmentation accuracies of over  $X\%$ .

**Graph-based methods.** Many segmentation and clustering algorithms use graph partitioning techniques [1] or normalized cuts for image segmentation [17, 38, 40]. The multicut graph partitioning algorithm extracts segments the graph and remove edges such that there are no cycles. This closely resembles the biological constraint that neurons have a topological genus of zero. There are several useful multicut heuristics which provide good approximations with reasonable computational costs [14, 20, 21]

**Skeletonization methods.** We use a graph-based abstraction of segmentation data based on skeletonizations. This topic is the focus of extensive research in the fields of computer graphics, mathematics, and biomedical visualization. Some of the research explores topologically consistent thinning algorithms and potential medical applications of these methods [30, 31]. In computer graphics, fast medial axis algorithms allow animators to quickly move characters through successive frames [2, 3]. In these works, the skeleton acts as the simplest representation of a 3-D volume. The Tree-structure Extraction Algorithm for Accurate and Robust Skeletons (TEASER) has been used by connectomics researchers to parameterize 3-D shapes [36, 43].

## 3. Method

There are two types of errors that can occur in image segmentation problems. The first, called a split error, occurs when there are two segments that should have been merged. The second, called a merge error, happens when one segment should be split into two. Generally, it is much more difficult to correct merge errors than to correct split errors (CITE). Our method takes as input an oversegmentation of an *EM* image volume where there are many more split errors than merge errors. Our goal is to identify locations of split errors and merge the corresponding segments. Section 4.1 discusses two pipelines for generating these segmentations.

From the input segmentation we generate a graph  $G$  with nodes  $N$  and edges  $E$  with weights  $w_e$ . The nodes correspond to label segments from the segmentation with edges between segments considered for merging. Ideally, our graph has edges corresponding to all of the segments which were erroneously split with few edges between correctly split segments. We generate a skeleton for every segment following the intuition that a skeleton represents a simplified representation of the overall shape of an object. We locate merge candidates and produce corresponding edges based on these skeletons. A CNN generates the edge weights by learning a merge function given two seg-

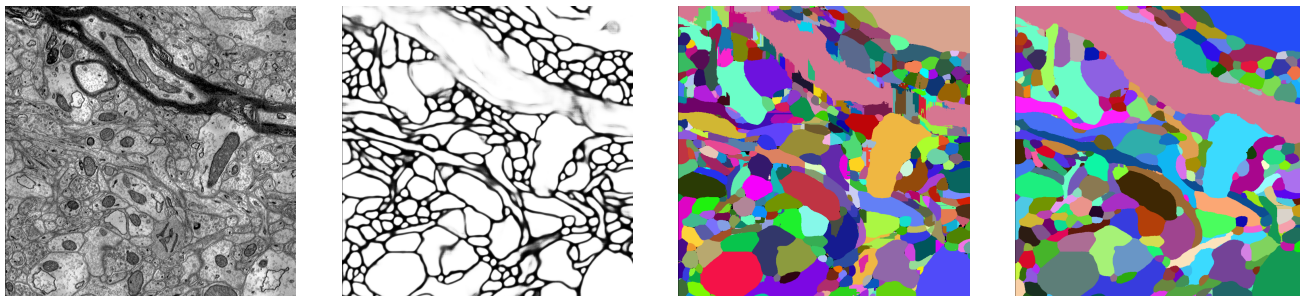


Figure 2: An overview of the existing methods. On the left is the original EM image data. A neural network (here VD2D3D) predicts the affinities between neighboring voxels. The Zwatershed algorithm clusters these voxels into supervoxels. NeuroProof agglomerates these supervoxels to create larger segments.

ments as input. A multicut heuristic generates a partition on the graph where nodes in the same partition are assigned the same output label. Thus there are three major components to our framework: skeletonization for constructing a graph, network training for determining edge weights, and graph-partitioning using a multicut heuristic algorithm. (INSERT FIGURE HERE)

### 3.1. Graph Creation

We generate nodes  $N$  and edges  $E$  to apply a graph-based optimization strategy for segmentation. In addition, these edges need non-negative weights.

#### 3.1.1 Node Generation

The simplest node generation strategy creates one node for every unique segment label in the input volume. However, some of the millions of labels in the volume correspond to very small regions. Usually these locations have noisy image data so the voxel-based methods could not provide enough information to generate a larger segment. It is difficult to extract useful shape features from these segments because of their small, and often random, shape. We prune these nodes from the graph by removing all segments with fewer than 20,000 voxels. On a typical connectomics dataset this only remove XX% of segments.

#### 3.1.2 Edge Generation

A naïve approach to generating edges produces an edge between all adjacent segments. Two segments  $l_1$  and  $l_2$  are considered adjacent if there is a pair of adjacent voxels where one has label  $l_1$  and the other has label  $l_2$ . NeuroProof and GALA consider all pairs of adjacent segments for merging. This method produces too many edges in the graph for us. Therefore we present the following algorithm to identify pairs of segments to consider merging.

First, we extract a skeleton from each segment using the TEASER algorithm [36, 43]. Figure 3 shows the skeletons

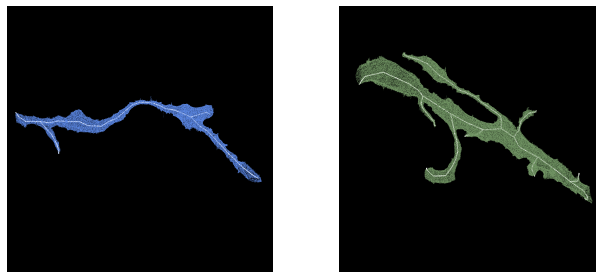


Figure 3: Two example outputs of the TEASER skeletonization algorithm.

in white of two segments from the label volume. These skeletons consist of a sequence of *joints*, locations that are a local maximum distance from the segment boundary, with line segments connecting successive joints. We prune the joints that are within 50 voxels of each other to reduce unnecessary branching. For the purposes of our algorithm, joints that have only one connected neighbor are referred to as *endpoints*. Many of the segments that are erroneously split follow a similar pattern (Figure 4). In these split instances the skeletons have nearby endpoints.

After skeletonization, we begin to identify segments for merge consideration with the following two-pass heuristic. In the first pass, we iterate over all endpoints  $e$  belonging to a segment  $S$  and create a set of segments  $S'_e$  that includes all labels that have a single voxel within  $t_{low}$  voxels from  $e$ . Elements of these sets are candidates for merging. However the first pass often has too many candidates that should remain split so we apply an additional pass for further pruning. In the second pass, we consider all of the segments  $S'_e$  for every endpoint  $e$ . If a segment  $S' \in S'_e$  has an endpoint within  $t_{high}$  voxels of  $e$ , the segment  $S$  and  $S'$  are considered for merging. We store the midpoint between the two endpoints as the “center” of the potential merge. Algorithm (ADD REF) provides pseudocode for this edge generation algorithm.

**function** GENERATEEDGES(*skeletons*)





Figure 4: Two erroneously split segments that should merge together. Most segments that we want to merge have the same general structure.

```

for skeleton in skeletons do
    candidates = set()
    for endpoint in skeleton do
        TODO ADD CODE
    end for
end for
end function

```

Note that this algorithm does not enforce any segment adjacency constraints. Figure (ADD FIGURE) shows two examples that would not be considered in NeuroProof or GALA since these algorithms only consider merging adjacent segments.

### 3.2. Edge Probabilities

The previous section outlines how to generate edges between nodes in our graph structure. Here we introduce a neural network architecture for generating probabilities that two nodes sharing an edge belong to the same neuron. The neural network takes as input only data from the input segmentation.

#### 3.2.1 Network Architecture

Our graph generation algorithm produces 3-D locations that require further consideration for merging. To determine which of these segments should actually merge, we train a 3-D CNN using the oversegmentation and the corresponding manually labeled ground truth data (Section 4.1). We extract a cubic region of interest around these locations as input to the CNN. These regions of interests will provide the local information for the neural network to predict which neighboring segments belong to the same neuron.

The networks receives three input channels for every voxel in the region of interest around segments  $l_1$  and  $l_2$ . The input to all of the channels is in the set  $\{-0.5, 0.5\}$ . The first channel is 0.5 only if the corresponding voxel has label  $l_1$ . The second channel is 0.5 only if the corresponding voxel has label  $l_2$ . The third channel is 0.5 if the corresponding voxel is either  $l_1$  or  $l_2$ .

Figure 5 provides an overview of our architecture. Our network architecture has three layers of double convolutions followed by a max pooling step following the work of Chatfield et al. that found such a framework improves on single convolution layers [5]. The first two max pooling layers are anisotropic with pooling only in the  $x$  and  $y$  dimen-

sions to account for the anisotropic nature of the datasets. The output after this final pooling step is flattened into a 1-D vector which is input into two fully connected layers. The final layer produces a probability with a sigmoid activation function [8]. All of the other activation functions are LeakyReLU [25]. We use a stochastic gradient descent optimizer with Nesterov’s accelerated gradient [27]. There are dropouts of 0.2 after every pooling layer and the first dense layer, and a dropout of 0.5 after the final dense layer. This prevents overfitting of the training data.

### 3.3. Agglomeration

After constructing the graph structure we apply a graph-based segmentation strategy. There are many formulations of graph-based optimization strategies that provide different guarantees on their output. Neurons in the brain should be acyclic, i.e. the output shape should have a genus of zero. Current connectomics agglomeration techniques do not leverage this additional information but rather consider neighboring regions in successive order without regard to loop creation. In our graph formulation we enforce this topological property by applying a multicut partition onto the graph that generates a *forest* on the nodes. A forest is a partitioning of a graph into a set of trees (i.e. no segment has a cycle). There are several heuristics that solve the multicut problem. For our purposes we use the Kernighan-Lin algorithm [20]. The running time of this algorithm is  $\mathcal{O}(N^3)$ , where  $N$  is the number of nodes in the graph (DOUBLE CHECK).

## 4. Evaluation

We evaluate our schema on two different connectomics datasets, one anisotropic and the other isotropic, from two different species.

### 4.1. Datasets

**Kasthuri.** The Kasthuri dataset images the neocortex of a mouse brain produced by a scanning electron microscope [18]. This dataset is  $5342 \times 3618 \times 338$  voxels in size. The resolution of the dataset is  $3 \times 3 \times 30 \text{ nm}^3$  per voxel. We evaluate our methods using the left cylinder of this 3-cylinder dataset. We downsample the dataset in the  $x$  and  $y$  dimensions to give a final resolution of  $6 \times 6 \times 30 \text{ nm}^3$  per voxel. We divide the dataset into two volumes along the  $x$  dimension. Thus, each volume is  $8.0 \times 10.9 \times 10.1 \mu\text{m}^3$ .

**FlyEM.** The FlyEM dataset comes from the mushroom body of a 5-day old adult male *Drosophila* fly imaged by a focused ion-beam milling scanning electron microscopy. The mushroom body of this species is the major site of associative learning [39]. The original dataset contains a  $40 \times 50 \times 120 \mu\text{m}^3$  volume of which we use two cubes of

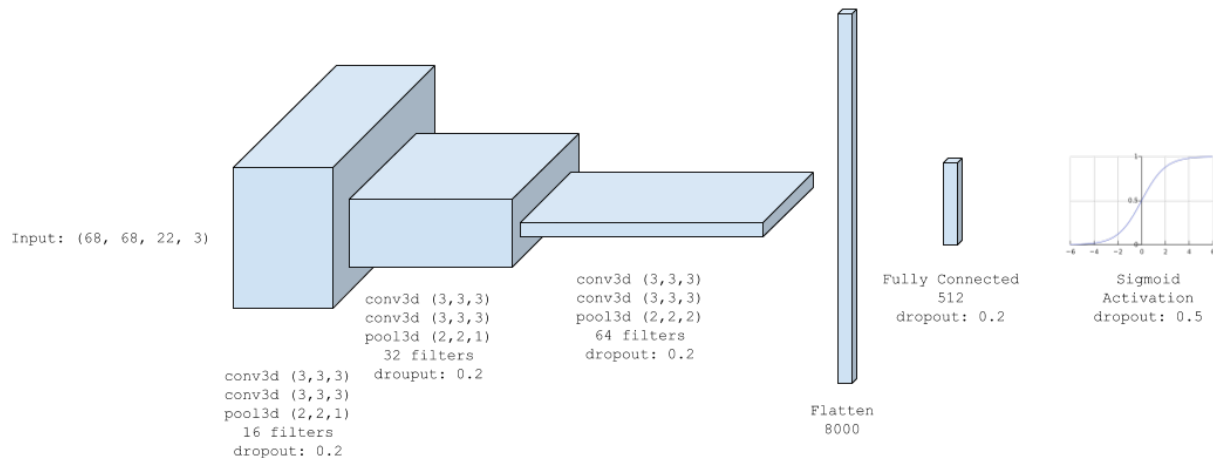


Figure 5: The architecture for the neural networks follows the *VGG* style of double convolutions followed by a max pooling operation. The number of filters doubles each layer leading to a fully connected layer and a sigmoid activation function.

size  $10 \times 10 \times 10 \mu\text{m}^3$ . The resolution of this dataset is  $10 \times 10 \times 10 \text{ nm}^3$  so each volume has 1000 voxels in each dimension.

**Segmentation Pipeline and Baseline.** The segmentation on the Kasthuri dataset was computed by agglomerating 3D supervoxels produced by *zwatershed* from 3D affinity predictions [44]. A recent study by Funke et.al. demonstrated superior performance of such method over existing ones on anisotropic data [37]. We learned 3d affinities in x,y,z using MALIS loss with a U-net [41, 35]. We apply the *zwatershed* algorithm, with suitable parameters, to compute an 3D over-segmentation of the volume. The resulting 3D over-segmentation is then agglomerated using the technique of context-aware delayed agglomeration to generate the final segmentation [32]. The VI values at different stopping thresholds of agglomeration correspond to the points on the curve plotted in Figure YYY.

We have collected two  $1000 \times 1000 \times 1000$  voxel ( $10 \times 10 \times 10 \mu\text{m}^3$ ) volumes from the authors [39]. Based on the authors' suggestion, we applied the context-aware delayed agglomeration algorithm [32] that shows improved performance on this dataset than the pipeline used in the original publication. This segmentation framework learns voxel and supervoxel classifiers with an emphasis to minimize under-segmentation error. At the same time this framework produces lower over-segmentation than standard algorithms. This algorithm first computes multi-channel 3D predictions for membranes, cell interiors, and mitochondria, among other cell features. The membrane prediction channel is utilized to produce an over-segmented volume using 3D *zwatershed*, which is then agglomerated hierarchically up to a certain confidence threshold. We used exactly same pa-

rameters for the publicly available code for this algorithm and used different agglomerations thresholds to plot the VI error curve.

## 4.2. Pruning via Skeletonization

We prune potential merge candidates by running Algorithm ?? on the input dataset. There are two essential parameters to the algorithm:  $t_{low}$  and  $t_{high}$ . Ideally, the merge candidates output by this algorithm will contains all possible positive examples with a very limited number of negative examples. After considering various thresholds, we find that  $t_{low} = 240 \text{ nm}$  and  $t_{high} = 600 \text{ nm}$  produces the best results given this objective function. Note that these thresholds are in nanometers and not voxels. Connectomics datasets often have different sample resolutions and downsampling in  $z$ . Using nanometers allows us to have uniform units across all of these datasets and calculate the thresholds in voxels at runtime. The thresholds are  $t_{low} = (40, 40, 8)$  voxels and  $t_{high} = (100, 100, 20)$  voxels for the Kasthuri dataset  $t_{low} = (24, 24, 24)$  voxels and  $t_{high} = (60, 60, 60)$  voxels for the FlyEM dataset. The thresholds are anisotropic or isotropic depending on the corresponding isotropy of the dataset. Table 2 shows the overall success of this method of candidate pruning.

## 4.3. Classifier Training

We use the Kasthuri Vol. 1 dataset for training and validation. We train on 80% of the potential merge candidates for this volume. The validation the neural network classifier on the remaining 20% of candidates. We consider networks with varying input sizes, optimizers, loss functions, filter sizes, learning rates, and activation functions. The supplemental material includes information on the experiments that determined these final parameters. Table 1 provides the

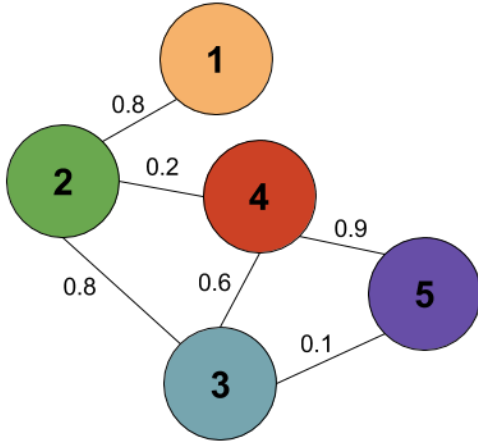


Figure 6: An example of the benefits of using multicut over simpler agglomeration schemes. If we input this example into a naïve agglomeration strategy that collapses all edges with a threshold greater than 0.5, this entire segment will merge together despite the fact that nodes 2 and 4 and nodes 3 and 5 have low affinities.

parameters in the final network. There are 7,294,705 learnable parameters in our final architecture. All the parameters are randomly initialized following the Xavier uniform distribution [9]. Training concluded after 34 epochs.

Parameters	Values
Loss Function	Mean Squared Error
Optimizer	SGD with Nesterov Momentum
Momentum	0.9
Initial Learning Rate	0.01
Decay Rate	$5 * 10^{-8}$
Activation	LeakyReLU ( $\alpha = 0.001$ )
Kernel Sizes	$3 \times 3 \times 3$
Filter Sizes	$16 \rightarrow 32 \rightarrow 64$

Table 1: Parameters for the CNN

**Data Augmentation.** We apply data augmentation to the generated examples to increase the size of the training datasets. We consider all rotations of 90 degrees along the  $xy$ -plane in addition to mirroring along the  $x$  and  $z$  axes. This produces 16 times more training data.

#### 4.4. Graph-based Strategies

Applying a top-down globally optimal partitioning function allows us to enforce some domain-specific constraints on the reconstruction. In connectomics, we want to enforce the topological restrictions that each partition in the graph has a genus of zero. The greedy-additive heuristic

Dataset	Baseline	After Pruning
Kasthuri Vol. 1	763 / 21242 (3.47%)	753 / 3459 (17.88%)
Kasthuri Vol. 2	1010 / 26073 (3.73%)	904 / 4327 (17.28%)
FlyEM Vol. 1	269 / 14875 (1.78%)	262 / 946 (21.69%)
FlyEM Vol. 2	270 / 16808 (1.58%)	285 / 768 (27.07%)

Table 2: The results of our pruning heuristic compared to the current baseline.

solves the multicut graph partitioning problem by enforcing this constraint. Previous agglomeration strategies at the per-region level consider neighboring superpixels in order of merge probability. These superpixels are clustered hierarchically without concern for global constraints. We compare the benefits of a top-down partitioning function versus the traditional bottom-up clustering methods.

#### 4.5. Variation of Information

We evaluate the performance of our methods using the split version of the variance of information [26]. Consider a ground truth labeling  $GT$  and our automatically reconstructed segmentation  $SG$ . Over and undersegmentation are quantified by the conditional entropy  $H(GT|SG)$  and  $H(SG|GT)$  respectively. Since we are measuring the entropy between two clusterings, better split variation of information scores are closer to the origin.

### 5. Results

#### 5.1. Pruning via Skeletonization

Table 2 shows the results of pruning using the skeletonization heuristic. The baseline algorithm considers all adjacent regions for merging. Our method removes a significant portion of these candidates while maintaining a large number of the true merge locations. This edge pruning is essential for the graph partitioning algorithms which have a computational complexity dependence on the number of edges (CHECK). Our pruning heuristic removes at least  $6 \times$  the number of edges between correctly split segments on all datasets, achieving a maximum removal ratio of  $20 \times$ . Equally important is the number of split errors that remain after pruning. These are the locations that we want to merge to create a more accurate reconstruction. For every dataset, the number of positive candidates remains relatively even. However, since our heuristic does not enforce an adjacency constraint of two regions when constructing edges in the graph, the difference does not indicate the number of examples excluded by pruning. In fact, our method finds a number of examples which are non-adjacent. Figure 7 shows two example segments which are split errors. The top example our algorithm missed but the segments are adjacent. The bottom example our algorithm found despite the fact that they are not adjacent.

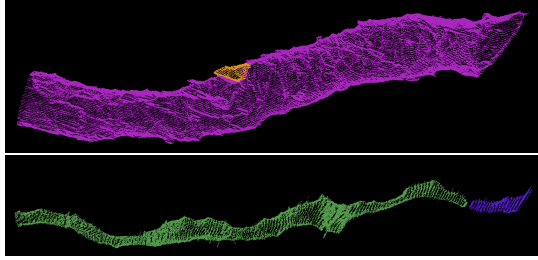


Figure 7: Example merge candidates.

Dataset	Precision	Recall	Accuracy
Kasthuri Training			
Kasthuri Testing			
FlyEM Vol. 1			
FlyEM Vol. 2			

Table 3: Precision and recall for the training and three test datasets.

## 5.2. Classification Performance

Table ?? shows the precision and recall for all of the datasets. Our methods are more general than traditional connectomics examples allowing us to train the network on an anisotropic dataset and get impressive results on an isotropic dataset. Our initial network does not take in any image data, only the segment shapes, so we merely extract the  $1200\text{nm}^3$  region from any dataset and rescale as input into the neural network. For each of the tables, the top left square gives the number of segments which should merge that we predict merge. The bottom right square gives the number of segments which should not merge that we predict should not merge. The bottom left quadrant indicates the amount of false positives, candidates which we predict merge which do not. The top right quadrant gives the amount of false negatives where we predict split although the candidates should merge. Figure 8 shows the receiver operating characteristic (ROC) curve for all four datasets.

## 5.3. Graph Based Strategies

Using a graph-based optimization strategy prevents XX segments from merging compared to the simple hierarchical agglomeration strategy with an optimal threshold cut off. Since correcting merge errors is significantly more difficult than correcting split errors, it is desirable to limit the number of false merges. The graph-based strategies significantly improve this error type.

## 5.4. Variation of Information Improvements

The final metric for comparing two connectomics segmentations is computing the variation of information with respect to an expert-labeled ground truth dataset. Figure 9

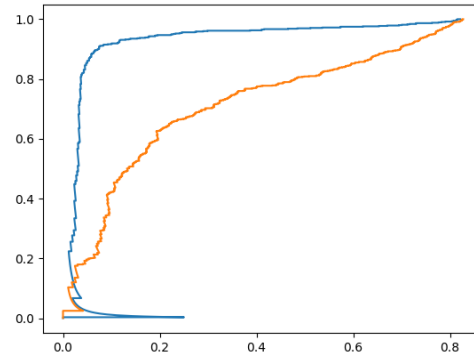


Figure 8: The receiver operating characteristic (ROC) curve for all four datasets.

shows the results on the datasets compared to the baseline (green) and an oracle (blue).

## 6. Conclusions

## References

- [1] B. Andres, T. Kroeger, K. L. Briggman, W. Denk, N. Korogod, G. Knott, U. Koethe, and F. A. Hamprecht. Globally optimal closed-surface segmentation for connectomics. In *European Conference on Computer Vision*, pages 778–791. Springer, 2012. 2
- [2] I. Baran and J. Popović. Automatic rigging and animation of 3d characters. In *ACM Transactions on Graphics (TOG)*, volume 26, page 72. ACM, 2007. 2
- [3] G. Bharaj, T. Thormählen, H.-P. Seidel, and C. Theobalt. Automatically rigging multi-component characters. In *Computer Graphics Forum*, volume 31, pages 755–764. Wiley Online Library, 2012. 2
- [4] J. A. Bogovic, G. B. Huang, and V. Jain. Learned versus hand-designed feature representations for 3d agglomeration. *arXiv preprint arXiv:1312.6159*, 2013. 1, 2
- [5] K. Chatfield, K. Simonyan, A. Vedaldi, and A. Zisserman. Return of the devil in the details: Delving deep into convolutional nets. *arXiv preprint arXiv:1405.3531*, 2014. 2, 4
- [6] D. Ciresan, A. Giusti, L. M. Gambardella, and J. Schmidhuber. Deep neural networks segment neuronal membranes in electron microscopy images. In *Advances in neural information processing systems*, pages 2843–2851, 2012. 2
- [7] R. W. Connors, M. M. Trivedi, and C. A. Harlow. Segmentation of a high-resolution urban scene using texture operators. *Computer Vision, Graphics, and Image Processing*, 25(3):273–310, 1984. 2
- [8] K.-I. Funahashi. On the approximate realization of continuous mappings by neural networks. *Neural networks*, 2(3):183–192, 1989. 4
- [9] X. Glorot and Y. Bengio. Understanding the difficulty of training deep feedforward neural networks. In *Proceedings*



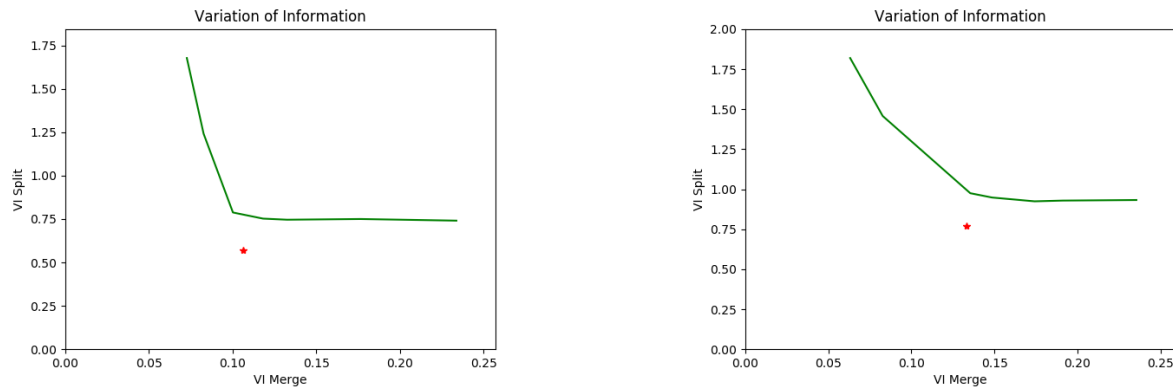


Figure 9: The improvement on variation of information from the baseline NeuroProof segmentation (green). Results closer to the origin are better.

- of the Thirteenth International Conference on Artificial Intelligence and Statistics, pages 249–256, 2010. 6
- [10] D. Haehn, J. Hoffer, B. Matejek, A. Suissa-Peleg, A. K. Al-Awami, L. Kametsky, F. Gonda, E. Meng, W. Zhang, R. Schalek, et al. Scalable interactive visualization for connectomics. In *Informatics*, volume 4, page 29. Multidisciplinary Digital Publishing Institute, 2017. 2
- [11] D. Haehn, V. Kaynig, J. Tompkin, J. W. Lichtman, and H. Pfister. Guided proofreading of automatic segmentations for connectomics. *arXiv preprint arXiv:1704.00848*, 2017. 2
- [12] D. Haehn, S. Knowles-Barley, M. Roberts, J. Beyer, N. Kasthuri, J. W. Lichtman, and H. Pfister. Design and evaluation of interactive proofreading tools for connectomics. *IEEE Transactions on Visualization and Computer Graphics*, 20(12):2466–2475, 2014. 2
- [13] D. G. C. Hildebrand, M. Cicconet, R. M. Torres, W. Choi, T. M. Quan, J. Moon, A. W. Wetzel, A. S. Champion, B. J. Graham, O. Randlett, et al. Whole-brain serial-section electron microscopy in larval zebrafish. *Nature*, 545(7654):345–349, 2017. 1
- [14] A. Horňáková, J.-H. Lange, and B. Andres. Analysis and optimization of graph decompositions by lifted multicuts. In *International Conference on Machine Learning*, pages 1539–1548, 2017. 2
- [15] V. Jain, B. Bollmann, M. Richardson, D. Berger, M. Helmstädter, K. Briggman, W. Denk, J. Bowden, J. Mendenhall, W. Abraham, K. Harris, N. Kasthuri, K. Hayworth, R. Schalek, J. Tapia, J. Lichtman, and S. Seung. Boundary learning by optimization with topological constraints. In *Proc. IEEE CVPR 2010*, pages 2488–2495, 2010. 2
- [16] M. Januszewski, J. Maitin-Shepard, P. Li, J. Kornfeld, W. Denk, and V. Jain. Flood-filling networks. *arXiv preprint arXiv:1611.00421*, 2016. 2
- [17] J. H. Kappes, M. Speth, G. Reinelt, and C. Schnörr. Higher-order segmentation via multicuts. *Computer Vision and Image Understanding*, 143:104–119, 2016. 2
- [18] N. Kasthuri, K. J. Hayworth, D. R. Berger, R. L. Schalek, J. A. Conchello, S. Knowles-Barley, D. Lee, A. Vázquez-Reina, V. Kaynig, T. R. Jones, et al. Saturated reconstruction of a volume of neocortex. *Cell*, 162(3):648–661, 2015. 1, 4
- [19] V. Kaynig, A. Vázquez-Reina, S. Knowles-Barley, M. Roberts, T. R. Jones, N. Kasthuri, E. Miller, J. Lichtman, and H. Pfister. Large-scale automatic reconstruction of neuronal processes from electron microscopy images. *Medical image analysis*, 22(1):77–88, 2015. 2
- [20] B. W. Kernighan and S. Lin. An efficient heuristic procedure for partitioning graphs. *The Bell system technical journal*, 49(2):291–307, 1970. 2, 4
- [21] M. Keuper, E. Levinkov, N. Bonneel, G. Lavoué, T. Brox, and B. Andres. Efficient decomposition of image and mesh graphs by lifted multicuts. In *Proceedings of the IEEE International Conference on Computer Vision*, pages 1751–1759, 2015. 2
- [22] S. Knowles-Barley, V. Kaynig, T. R. Jones, A. Wilson, J. Morgan, D. Lee, D. Berger, N. Kasthuri, J. W. Lichtman, and H. Pfister. Rhoanet pipeline: Dense automatic neural annotation. *arXiv preprint arXiv:1611.06973*, 2016. 1, 2
- [23] S. Knowles-Barley, V. Kaynig, T. R. Jones, A. Wilson, J. Morgan, D. Lee, D. Berger, N. Kasthuri, J. W. Lichtman, and H. Pfister. Rhoanet pipeline: Dense automatic neural annotation, 2016. (available on arXiv:1611.06973 [cs.CV]). 2
- [24] K. Lee, A. Zlateski, V. Ashwin, and H. S. Seung. Recursive training of 2d-3d convolutional networks for neuronal boundary prediction. In *Advances in Neural Information Processing Systems*, pages 3573–3581, 2015. 1, 2
- [25] A. L. Maas, A. Y. Hannun, and A. Y. Ng. Rectifier nonlinearities improve neural network acoustic models. In *Proc. ICML*, volume 30, 2013. 2, 4
- [26] M. Meila. Comparing clusterings by the variation of information. In *Colt*, volume 3, pages 173–187. Springer, 2003. 6
- [27] Y. Nesterov. A method of solving a convex programming problem with convergence rate  $O(1/k^2)$ . 2, 4



- [28] J. Nunez-Iglesias, R. Kennedy, S. M. Plaza, A. Chakraborty, and W. T. Katz. Graph-based active learning of agglomeration (gala): a python library to segment 2d and 3d neuroimages. *Frontiers in neuroinformatics*, 8, 2014. 1, 2
- [29] R. Osada, T. Funkhouser, B. Chazelle, and D. Dobkin. Shape distributions. *ACM Transactions on Graphics (TOG)*, 21(4):807–832, 2002. 2
- [30] K. Palágyi. A 3d 3-subiteration thinning algorithm for medial surfaces. In *International Conference on Discrete Geometry for Computer Imagery*, pages 406–418. Springer, 2000. 2
- [31] K. Palágyi, E. Balogh, A. Kuba, C. Halmai, B. Erdőhelyi, E. Sorantin, and K. Haussegger. A sequential 3d thinning algorithm and its medical applications. In *Biennial International Conference on Information Processing in Medical Imaging*, pages 409–415. Springer, 2001. 2
- [32] T. Parag, A. Chakraborty, S. Plaza, and L. Scheffer. A context-aware delayed agglomeration framework for electron microscopy segmentation. *PLOS ONE*, 10(5):1–19, 05 2015. 5
- [33] T. Parag, F. Tschopp, W. Grisaitis, S. C. Turaga, X. Zhang, B. Matejek, L. Kamensky, J. W. Lichtman, and H. Pfister. Anisotropic em segmentation by 3d affinity learning and agglomeration. *arXiv preprint arXiv:1707.08935*, 2017. 1, 2
- [34] X. Ren and J. Malik. Learning a classification model for segmentation. In *null*, page 10. IEEE, 2003. 2
- [35] O. Ronneberger, P. Fischer, and T. Brox. U-net: Convolutional networks for biomedical image segmentation. In *International Conference on Medical Image Computing and Computer-Assisted Intervention*, pages 234–241. Springer, 2015. 1, 2, 5
- [36] M. Sato, I. Bitter, M. A. Bender, A. E. Kaufman, and M. Nakajima. Teasar: Tree-structure extraction algorithm for accurate and robust skeletons. In *Computer Graphics and Applications, 2000. Proceedings. The Eighth Pacific Conference on*, pages 281–449. IEEE, 2000. 2, 3
- [37] P. Schlegel, M. Costa, and G. S. Jefferis. Learning from connectomics on the fly. *Current Opinion in Insect Science*, 2017. 5
- [38] J. Shi and J. Malik. Normalized cuts and image segmentation. *IEEE Transactions on pattern analysis and machine intelligence*, 22(8):888–905, 2000. 2
- [39] S.-y. Takemura, Y. Aso, T. Hige, A. Wong, Z. Lu, C. S. Xu, P. K. Rivlin, H. Hess, T. Zhao, T. Parag, et al. A connectome of a learning and memory center in the adult drosophila brain. *Elife*, 6, 2017. 4, 5
- [40] S. Tatiraju and A. Mehta. Image segmentation using k-means clustering, em and normalized cuts. *Department of EECS*, 1:1–7, 2008. 2
- [41] S. Turaga, K. Briggman, M. Helmstaedter, W. Denk, and S. Seung. Maximin affinity learning of image segmentation. In *Advances in Neural Information Processing Systems 22*. 2009. 5
- [42] A. Vázquez-Reina, M. Gelbart, D. Huang, J. Lichtman, E. Miller, and H. Pfister. Segmentation fusion for connectomics. In *Proc. IEEE ICCV*, pages 177–184, Nov 2011. 2
- [43] T. Zhao and S. M. Plaza. Automatic neuron type identification by neurite localization in the drosophila medulla. *arXiv preprint arXiv:1409.1892*, 2014. 2, 3
- [44] A. Zlateski and H. S. Seung. Image segmentation by size-dependent single linkage clustering of a watershed basin graph. *arXiv preprint arXiv:1505.00249*, 2015. 1, 2, 5
- [45] J. Zung, I. Tartavull, and H. S. Seung. An error detection and correction framework for connectomics. *CoRR*, abs/1708.02599, 2017. 2